https://doi.org/10.5194/egusphere-2024-3316
Preprint. Discussion started: 4 November 2024

Light scattering and microphysical properties of atmospheric bullet rosette ice crystals

Shawn W. Wagner[1,*], Martin Schnaiter[1,2], Guanglang Xu[1], Franziska Nehlert[1], and Emma Järvinen[1,**]
[1]Karlsruhe Institute of Technology, Karlsruhe, Germany
[2]schnaiTEC GmbH, Bruchsal, Germany
[*]Now at University of North Dakota, Grand Forks, United States
[**]Now at University of Wuppertal, Wuppertal, Germany
Correspondence: Shawn W. Wagner (shawn.wagner@und.edu), and/or Emma Järvinen (jaervinen@uni-wuppertal.de)

Abstract. Cirrus clouds play a critical role in the Earth's radiative budget. The extent of the radiative impact of cirrus clouds is determined by a number of their physical properties, such as aspherical ice crystal composition. One of the most relevant cirrus ice crystal habits is a polycrystalline bullet rosette, where individual bullets are radiating from the same nucleation point. Here, the link between the crystal morphology of atmospheric bullet rosettes and their asymmetry parameter (g) is experimentally investigated using correlated high resolution in situ stereo-images of individual rosettes and their angular scattering functions measured by the airborne Particle Habit Imaging and Polar Scattering (PHIPS) cloud probe. Bullet rosette stereo-images are analyzed for their microphysical properties, including maximum dimension, bullet aspect ratio, number of bullets, projected area, bullet hollowness, derived mass, derived effective density and derived terminal velocity, as well as their optical properties such as g and optical complexity parameter. Results indicate that much lower g values represent real atmospheric bullet rosette crystals than what is expected by numerical calculations assuming solid or hollow bullets with smooth idealized surfaces, indicating higher levels of crystal complexity than have been previously incorporated within bullet rosette ray-tracing models.

1 Introduction

Cirrus clouds have been found to cover the Earth's surface at a global average of approximately 40 % (Sassen et al., 2008; Lynch, 1996; Wylie et al., 1994). Due to their high frequency of occurrence, as well as being one of the first solid encounters of photons when entering the Earth's atmosphere, cirrus clouds have a major impact on the Earth's radiative budget (Paltridge, 1980; Liou, 1986). The extent of this impact is determined, in part, by the aspherical ice crystal single scattering properties within the cirrus. Therefore, an understanding of the crystal single scattering properties is necessary to understand the full extent of this impact, which in turn improves climatological and radiative modeling capabilities.

One of the most comprehensive and widely accepted habit diagrams at present time, produced by Bailey and Hallet (2009), suggests that the low temperatures and range of supersaturations found within cirrus clouds are ideal conditions for forming the polycrystalline ice habit known as a bullet rosette (Heymsfield and Iaquinta, 2000; Heymsfield et al., 2002). Bullet rosettes and other rosette based polycrystals have (recently) been shown to comprise over half of the contents of in situ formed cirrus clouds (Lawson et al., 2019). While their frequency has been realized in more modern studies, bullet rosettes were first noted as

https://doi.org/10.5194/egusphere-2024-3316
Preprint. Discussion started: 4 November 2024

being observed in cloud by the work of Weikmann (1947). Since then significant technological advancements have been made regarding in situ measurement techniques, allowing for numerous studies to be conducted involving bullet rosettes such as Lawson et al. (2006, 2010, 2019), Um and McFarquhar (2007), Um et al. (2015), and many others. Um et al. (2015) conducted an in-depth microphysical analysis of several ice crystals using the Cloud Particle Imager (CPI) and data sets from three campaigns. It was found that bullet rosettes most frequently formed at temperatures of approximately -45 °C and had a mean number of bullets per rosette at 5.5 $\pm$ 1.35 with an increasing bullet aspect ratio as the number of bullets per rosette increased. Dimensions of bullet rosettes ranged from 80 μm at -65 °C to 300 μm at -30 °C, with dimensions generally increasing with increasing temperature. A number of studies of have also been conducted to quantify the mass and effective density of bullet rosettes (Brown and Francis, 1995; Heymsfield et al., 2002; Baker and Lawson, 2006; Um and McFarquhar, 2011; Erfani and Mitchell, 2016; Fridlind et al., 2016). Fridlind et al. (2016) has shown a strong correlation between calculated bullet rosette mass and the rosette maximum dimension using CPI images taken during the Small Particles in Cirrus (SPARTICUS) campaign, and provided a detailed comparison of these results to earlier works. Fridlind et al. (2016) found masses ranging from 0.001 to 0.1 mg for maximum dimensions ranging from 200 to 1100 μm. Additionally, correlations between effective density and maximum dimension as well as terminal velocity and maximum dimenesion were also found. Densitities ranged from 0.1 to 0.5 $\mathrm{g\,cm^{-3}}$ for rosettes with a maximum dimension between 200 to 1100 μm, with terminal velocities up to 210 $\mathrm{cm\,s^{-1}}$ for a maximum dimension of 1000 μm. This study aims to further build on previous work utilizing high resolution cloud particle imagers by increasing the accuracy of the bullet rosette microphysical parameterizations and relating the measured single-scattering properties of the same analyzed bullet rosettes.

Particle images taken across the multitude of studies on bullet rosettes show an inherently complex microphysical structure which directly impacts their single scattering properties. Yet, previous studies have been performed to analyze the shortwave optical properties of bullet rosettes using idealized ray-tracing models, such as Iaquinta et al. (1995) and Schmitt et al. (2006). Iaquinta et al. (1995) found that, assuming a random spatial orientation, the number and configuration of bullets per rosette have little effect on the overall angular scattering phase function (aside from an increase in the amount of side scattering with increasing numbers of bullets and bullet aspect ratios). Rather, other microphysical properties of the rosette such as the crystal size, cross section, projected area, bullet aspect ratios, etc., were determined to likely be important factors relating to cirrus radiative properties. Given a preferred orientation, the angular scattering function will differ significantly depending on the configuration of the bullets. Asymmetry parameters (g) were found to range from 0.788 to 0.876, depending on the aspect ratio of the individual bullets. Schmitt et al. (2006) extended this work to include bullet rosettes with varying degrees of hollowness. It was determined that "...hollow bullet rosettes have distinctly different scattering properties than do solid bullet rosettes". With compact (aspect ratio = 1) solid bullets, there was found to be a 13 % difference in g versus when the bullets are entirely hollow with g increasing with hollowness. For more elongated (aspect ratio = 0.1) bullets this difference is reduced to 3.5 % with g decreasing with hollowness. Here we move from light scattering by idealized model rosettes to in situ measured rosette light scattering properties, thus expanding from theoretical calculations to atmospheric observations.

In radiative transfer and climatological modeling, g is a crucial component. Thus, an understanding of g associated with real ice crystal habits is critical for a proper simulation of cirrus cloud effects on the Earth's radiative budget. In situ atmospheric

https://doi.org/10.5194/egusphere-2024-3316
Preprint. Discussion started: 4 November 2024

bullet rosette g values measured during the Cirrus in High Latitudes (CIRRUS-HL) airborne campaign are addressed in this study, along with ray-tracing results of bullet rosettes modeled after the microphysical properties found herein with varying degrees of simulated surface roughness.

2 Methodology

2.1 Airborne Measurements

CIRRUS-HL was an airborne mission based in Oberpfaffenhofen, Germany, to measure microphysical and radiative properties relating to high-latitude cirrus clouds using the High Altitude and Long Range (HALO) research aircraft. While the focus was intended to be northerly by sampling in subarctic Europe, pandemic restrictions in base location required focus to shift towards Central and Southern Europe. Both in situ and liquid origin cirrus (Krämer et al., 2016), as well as aviation related contrail cirrus were targeted. CIRRUS-HL consisted of twenty-four flights (one test flight, one calibration flight, and twenty-two research flights) from June 6^{th} to July 28^{th} 2021, accumulating a total of 140 research flight hours; twenty-one of the twenty-two research flights showed the presence of bullet rosettes. A suite of instruments for cloud microphysical and atmospheric state variables was deployed duing CIRRUS-HL (DLR, 2024), including the Particle Habit Imaging and Polar Scattering (PHIPS) cloud probe.

To experimentally investigate the habit-specific angular light scattering properties of atmospheric ice crystals, a single-particle nephelometer is combined with a high-resolution imaging system in PHIPS (Abdelmonem et al., 2016; Schnaiter et al., 2018). This setup allows for the identification and selection of ice crystals with specific habits, such as bullet rosettes, from an ensemble of crystals measured during flight legs in natural cirrus clouds. By isolating the scattering functions attributed to a specific habit, it is possible to derive that crystal's ensemble-averaged scattering function. In essence, this analysis method generates an artificial cloud composed solely of specific ice habits (e.g., bullet rosettes) based on measurements from real atmospheric ice crystals.

Upon entering the $\approx 0.3\ \mathrm{mm}^3$ detection volume of the PHIPS, a cloud particle scatters a continuous wave green laser with a wavelength of 532 nm which is registered by the trigger system. Twenty off-axis parabolic mirrors redirect scattered light to corresponding channel optical fibers in the 18° to 170° range, with an 8° resolution. Each mirror has a diameter of 10 mm and is positioned 83 mm from the sample volume, giving a solid angle of 0.011 sr. A multi-anode photomultiplier tube (MAPMT) converts received light into a current pulse. The pulse is then digitzed to a dynamic range of 2047 counts. A maximum sample rate of 9 kHz allows for rapid data acquisition in environments with high cloud particle concentrations.

Simultaneously, two charge-coupled device (CCD) cameras with telescopic assemblies record 1360 by 1024 pixel brightfield images of the cloud particle at a maximum acquistion rate of 10 Hz. The camera assemblies are positioned on either side of the sample volume with a 60° viewing angle of the particle (120° between the cameras). For the magnification settings used in CIRRUS-HL, focussed microscopes provide a pixel resolution of $\approx 1.61\ \mu\mathrm{m}$ with a maximum particle size range between 1650 - 2200 $\mu\mathrm{m}$ depening on particle orientation. Illumination is provided for 10 ns by an inchoherent 690 nm pulsed diode laser which eliminates wave interference and allows for clear, high resolution images. It is important to note that the

https://doi.org/10.5194/egusphere-2024-3316
Preprint. Discussion started: 4 November 2024

resolution is limited by the lens system rather than the pixel size, resulting in an optical resolution of approximately 6 μm at the magnification setting of 4 used in CIRRUS-HL. For further details on the PHIPS physical design and principles of operation, see Abdelmonem et al. (2016). For information on the PHIPS characterization and initial results, see Schnaiter et al. (2018).

2.1.1 Microphysical Analysis

PHIPS stereo-image pairs from CIRRUS-HL are manually reviewed and each imaged ice crystal is classified by their respective habit. Bullet rosettes are then selected for use in this study by assessing their image clarity, and if the crystal has been fully captured by at least one camera. Of the 5668 total bullet rosettes encountered during CIRRUS-HL, 4512 rosettes are accepted for this study. These bullet rosettes were entirely captured in at least one of the two PHIPS camera focal planes allowing for measurment of the maximum dimension with a high confidence. Of the 4512 bullet rosettes accepted, 1292 are found to have individually identifiable and distinguishable bullets, allowing for further analysis of the bullet related microphysical properties to be performed. These 1292 bullet rosettes will be the primary focus of the microphysical results and discussion. Aditionally, of the 5668 bullet rosettes encountered, a criteria was set to select rosettes with angular scattering functions in which no saturation of the first two PHIPS measurement channels occured. This resulted in a set of 1549 rosettes, only 1.4 % of which had at least one saturated channel between 34° and 170°. These rosettes will be the focus of the single-scattering properties results and discussion.

Bullet rosettes are further separated into categories based on the presence of cavities or air pockets. These subcategories are: solid, hollow, and inclusions. Examples of each category can be seen in Fig. 1. Solid bullet rosettes are defined as rosettes with bullets having no visible cavities or air pockets; hollow bullet rosettes consist of bullets with cavities which begin at the outward end of the bullets and move inward forming a convex opening which can span any length of the affected bullet (Schmitt and Heymsfield, 2007; Yang et al., 2008); inclusion rosettes have bullets which contain pockets that do not breach the outward ends of the bullets. Despite careful visible analysis of each available bullet rosette, not all images provide enough detail to determine if a bullet rosette is able to be placed into one of the aforementioned categories. While those rosettes are still included in the overarching group of all rosettes, they are excluded from further categorization. An example of a bullet rosette with an unknown categorization can also be seen in Fig. 1. These categories are specifically important for understanding the single-scattering properties results and discussion. If a rosette contains elements of multiple categories (such as both hollowness and inclusions), that rosette is only included in the overarching group of all rosettes.

Microphysical analysis of the individual bullets is conducted manually using MATLAB GUI based software to display the rosette images. Using the software, bullet number per rosette and the pixel locations of the individual bullet endpoints in terms of both length and width are visually determined and selected. Bullet length (L_B) is defined as the number of pixels between the rosette origin and the outward end of the bullet. Bullet width (W_B) is the number of pixels between the opposing bullet facets. Individual bullet aspect ratios (AR_B) are defined as:

$$AR_B = \frac{W_B}{L_B}. \tag{1}$$

https://doi.org/10.5194/egusphere-2024-3316
Preprint. Discussion started: 4 November 2024

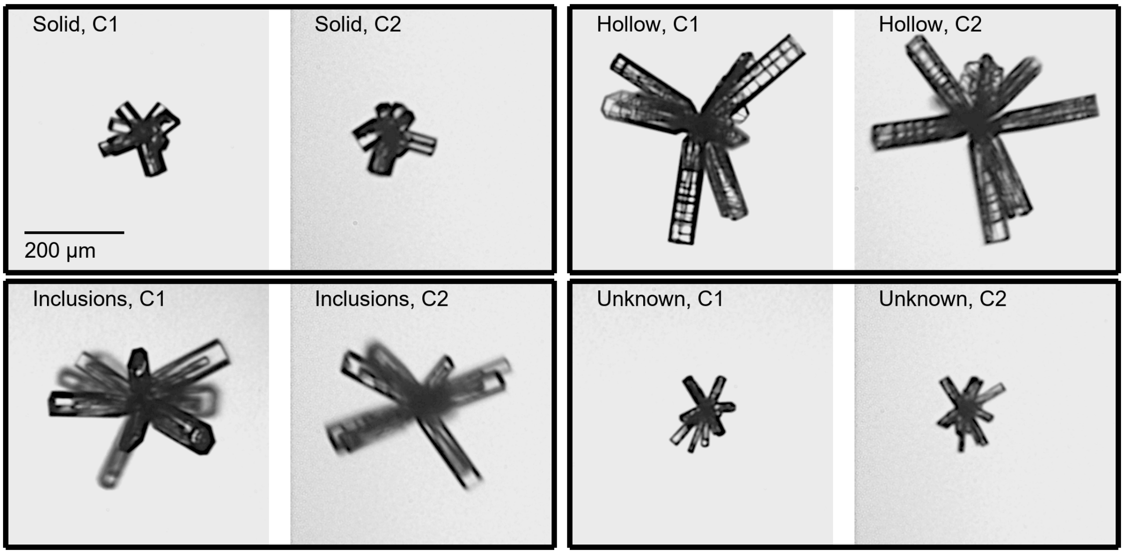

Figure 1. Example bullet rosettes imaged by the Particle Habit Imaging and Polar Scattering (PHIPS) probe, separated into categories based on the presence of cavities or air pockets. Camera assembly one (C1) images are on the left, and camera assembly two (C2) images are on the immediate right. There is a 120° separation between C1 and C2.

Corrections which account for errors due toL_B and W_B being assesed from bullet rosette projections on 2-D images are addressed in Appendix B. The hollowness factor is then calculated using the method of Schmitt et al. (2006). The same procedure is performed on hollow rosettes to indicate pixel locations for the beginning of hollowness (the edge of the bullet) and the end of the hollowness (a point within the bullet).

$$H_{FACTOR} = \frac{L_H}{L_B}, \tag{2}$$

where L_H is the length of the hollowness.

The maximum dimension (D_{max}) of each bullet rosette is included in the microphysical analysis using IDL image analysing software that is applied during the primary data processing, and has no corrections applied (Schön, 2011). The mass of each rosette is calculated by treating each bullet as a hexagonal column with a hexacone cap, with the H_{FACTOR} accounted for when applicable. Bullet rosette mass is represented as:

$$m = \rho_{ice} \times \overline{V_B} \times N_B, \tag{3}$$

where ρ_{ice} is the density of ice and is assumed to be 0.917 $\mathrm{g\ cm^{-3}}$, $\overline{V_B}$ is the average bullet volume for that rosette, and N_B is the number of bullets. Detailed equations pertaining to $\overline{V_B}$ can be found within Appendix B. Using the calculated bullet rosette mass, the effective density of each rosette is calculated using:

$$\rho_e = \frac{6m}{\pi D_{max}^3}. \tag{4}$$

https://doi.org/10.5194/egusphere-2024-3316
Preprint. Discussion started: 4 November 2024

Using methods outlined in Mitchell (1996) calculated bullet rosette mass with the measure bullet rosette projected area (A) can also be used to calculate the terminal velocity of each rossette:

$$V_t = \sqrt{\frac{2mg_c}{\rho_a A C_D}}, \tag{5}$$

where g_c is the gravitational constant (9.81 $\mathrm{m\,s^{-2}}$), ρ_a is the density of air and C_D is the drag coefficient. Detailed equations pertaining to ρ_a and C_D can be found within Appendix C.

2.1.2 Single-Scattering Property Retrievals

As with any polar nephelometer, calculating g from PHIPS measurements requires a retrieval algorithm to account for the limited angular range of the instrument. The methods applied in this study have been thoroughly described for g by Xu et al. (2022a). In the process of determining a method for retrieving g, Xu et al. (2022a) introduced an optical complexity parameter (C_p): a description of the isotropic degree of a scattering function which strongly correlates to g (Xu et al., 2023). This can be calculated using (Xu et al., 2022b):

$$C_p = (\sum_{l=0}^{\infty} |\hat{c}_{GO,l}|)^{-1}, \tag{6}$$

where $\hat{c}_{GO,l}$ is the expansion coefficients of the geometric optics phase function using a series of Legendre polynomials. These expansion coefficients are used in the g retrieval as well.

While g can range from -1 to 1, C_p only ranges from 0 to 1; 0 indicates a delta function and 1 indicates perfectly isotropic scattering. Thus, the angular scattering function becomes more featureless with increasing values of C_p. (Xu et al., 2022b) showed that C_p correlates with the complexity parameters used in ray-tracing models, and therefore we refer to it as an optical complexity parameter. A summarized case study of C_p as applied to rimed particles measured by the PHIPS can be found in Xu et al. (2022b). It should be noted that C_p is derived from the PHIPS measured angular scattering function, not from the stereo-images. As will be shown in Sect. 3.2, a C_p - g relation is useful when comparing the PHIPS measurements to the results of optical models.

2.2 Numerical Simulations

Numerical ray-tracing simulations are performed to compare the PHIPS bullet rosette g measurements from CIRRUS-HL to those of modeled rosettes, using solid rosette, hollow rosette and solid column geometries with the geometrical optics method of Macke et al. (1996). Crystal complexity is incorporated using the uniform tilted angle (UTA) method of Macke et al. (1996) to simulate crystal distortion, with distortion parameters (δ) including 0.0 (no distortion), 0.3, 0.6 and 0.9 (high distortion). It should be kept in mind that a δ value of 0.9 corresponds to an extreme shape distortion, which likely is an unphysical shape for natural ice cyrstals. Each crystal distortion was applied to ray-tracing simulations for the three crystal habits modeled for five area equivalent diameters (D) corresponding to the PHIPS size bins: 60 µm, 80 µm, 125 µm, 175 µm, and 225 µm. Additionally, a tilt angle distribution following the frequently utilized Gaussian tilted angle distribution (GTA) (e.g. Liou et al. (1998); Yang

https://doi.org/10.5194/egusphere-2024-3316
Preprint. Discussion started: 4 November 2024

and Liou (1998); Yang et al. (2013); Liu et al. (2013)) method is also applied for solid columns. In the case of the GTA approach, the complexity parameter (σ^2) is adjusted between 0.1 and 0.9 in incremements of 0.1 for each size group. Thus, the total number of ray-tracing simulations is 120. The length and width of the bullets and columns are varied to maintain AR_B of 0.2 while adjusting D. Both the solid and hollow bullet rosette simulations are based on a single bullet configuration with seven bullets. Bullets of the hollow rosette each have an H_{FACTOR} of 0.9. An additional form of crystal complexity in numerical ray-tracing can be achieved by simulating the optical effects of internal inclusions. This is done by artificially generating a scattering event after a certain distance, or mean free path (MFP), within the crystal is traveled (Macke et al., 1996). Though not considered for bullet rosettes, simulations of varying MFP were performed for cloumns. The simulated light wavelength is 532 nm to match that of the PHIPS. A single scattering abledo of 1, ray density of 0.03, 13 internal reflections, and 8 ray recursions with 10 000 crystal orientations are used with all values chosen to minimize the model runtime while maintaining realistic scattering conditions. The standard ice refractive index of 1.31 is also applied (Warren, 1984).

3 Results and Discussion

3.1 Microphysical Properties

Figure 2 gives an overview of the CIRRUS-HL cloud habit fraction as a function of temperature at the time of the measurment. For the CIRRUS-HL campaign as a whole, bullet rosettes comprise an average 15 $\%$ of all cloud particles at temperatures less than -45 °C. As the temperature increases the high frequency of bullet rosettes steadily decreases, and is partly replaced with side planes (polycrystals with plates extending outward from a central point) and mixed rosettes (rosettes containing both columns and plates). This is due to warmer environments (-10 °C > T > -40 °C) being conducive to plate-like growth regimes as opposed to the columnar regime dominate colder temperatures (T < -40 °C) (Bailey and Hallet, 2009). Temperatures from -40 to -50 °C consisted of 11 $\%$ bullet rosettes, which agrees well with the Lawson et al. (2019) findings on the frequency of bullet rosettes and bullet rosette polycrystals in clouds of the same temperature. However, the results of this study indicate temperatues of -50 to -60 °C containing 19 $\%$ bullet rosettes, while Lawson et al. (2019) found only 10 $\%$ in that temperature range. As Lawson et al. (2019) used data from the Airborne Tropical TRopopause EXperiment (ATTREX) which often sampled cirrus from convective outflow, this discrepency may be the result of the Lawson et al. (2019) crystals having been generated by convective processes rather than in situ origin cirrus. In our study both in situ and convective (liquid) origin cirrus were measured. While the formation of bullet rosettes is most common at temperatures less than -40 °C (Bailey and Hallet, 2009), they were found at temperatures as low as -25 °C. It should be noted that during all but one flight, bullet rosettes occurred at mean temperatures lower than -40 °C and most frequently at temperatures between -45 °C and -50 °C. This strongly agrees with the findings of Um et al. (2015). The relative humidity with respect to ice at the time of sampling varied between 85 $\%$ and 145 $\%$ (not shown), and does not indicate a strong relation to the presence of bullet rosettes as temperature does.

Stereo examples of the bullet rosettes chosen for analysis can be seen in Fig. 3 with their associated C_p value (further discussed in the following subsection). The analyzed rosettes have primarily asymmetrical bullet configurations, and frequently there are bullets of varying lengths and AR_B on a single rosette. These variations can also be seen numerically in Fig. 4, which

https://doi.org/10.5194/egusphere-2024-3316
Preprint. Discussion started: 4 November 2024

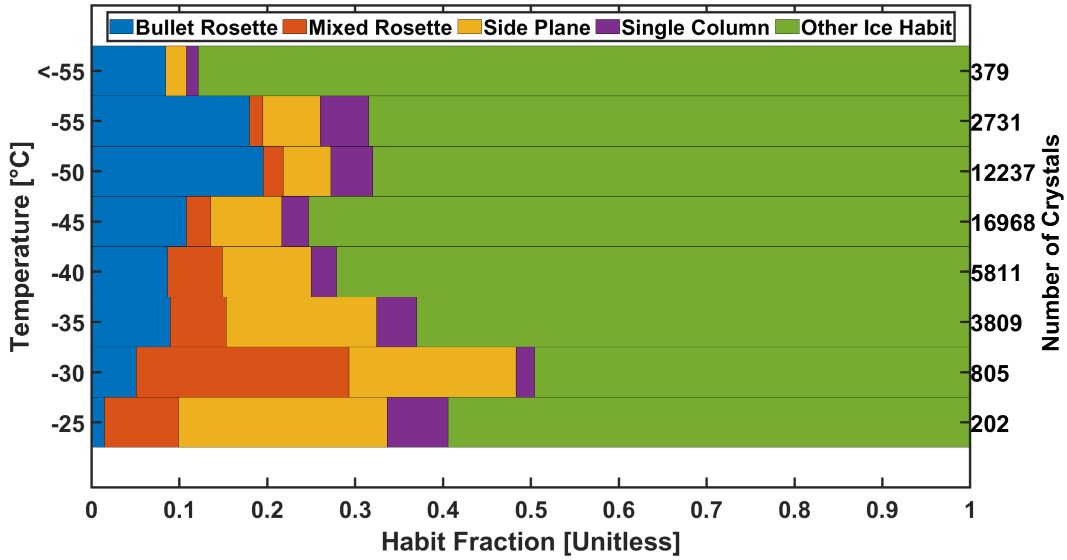

Figure 2. Habit fractions of various ice crystals that were both imaged and had their light scattering properties measured by the Particle Habit Imaging and Polar Scattering (PHIPS) probe during the Cirrus in High Latitudes (CIRRUS-HL) airborne campaign. The sampled ice crystals are grouped by temperatures from less than -50 °C to greater than -35 °C in 2.5 °C increments. Numbers on the right y-axis indicate the total number of sampled particles per temperature bin.

shows boxplots indicating the bullet rosette maximum dimensions for the 5668 accepted bullet rosettes, and the bullet AR_B, number of bullets per rosette, and H_{FACTOR} for the 1292 rosettes selected for a bullet analysis. As in Fig. 4, the bullet rosettes were examined in relation to both relative humidity with respect to ice as well as condensable water vapor (not shown). However, no further trends than those about to be outlined with relation to temperature were found.

Bullet rosette maximum dimensions for 5668 accepted rosettes range from 20 µm to 925 µm, with the median maximum dimensions spanning from 200 µm to 420 µm. While fairly consistent at temperatures below -35 °C, the median maximum dimension abruptly increases at -35 °C and warmer. The range of medians for only the rosettes accepted for further analysis (indicated with black dots) is higher at 300 µm to 525 µm. This can be explained by a bias owing to larger rosettes being more likely to have bullets which are confidently analyzable. When considering all acceptable bullet rosettes, the median maximum dimension is equal to or less than 420 µm at all analyzed temperatures, which agrees with Um et al. (2015). AR_B of individual bullets extend from a minimum of 0.1 to a maximum of 0.45, and the median AR_B remains fairly consistent at approximately 0.25 across most observed temperatures. A source of uncertainty for the visually based analysis is the potential inaccuracy in manually selecting the pixels for the outer edge and inner point of the individual bullets. Naturally, the objective is to be as close as possible to the outer edge of the bullet as well as the central origin point within the rosette. While identifying the outer edge is rather simple, Figs. 1 and 3 show how the point of origin is rarely well defined and often leads to an estimation as to the pixel location. However, the estimation that is made is assumed to be fairly reliable as examining the position of all

https://doi.org/10.5194/egusphere-2024-3316
Preprint. Discussion started: 4 November 2024

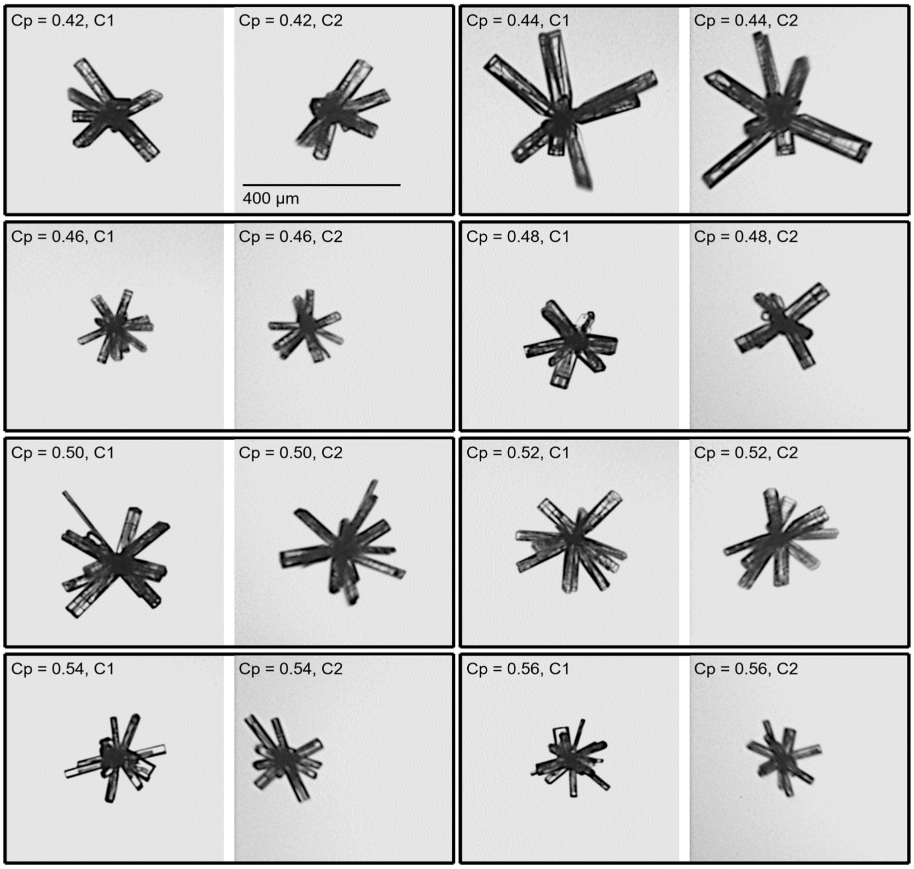

Figure 3. Bullet rosettes sampled during the Cirrus in High Latitudes (CIRRUS-HL) airborne campaign by the Particle Habit Imaging and Polar Scattering (PHIPS) probe, with camera assembly one (C1) images on the left, and camera assembly two (C2) images on the immediate right. There is a 120° separation between C1 and C2. The images are sorted in order of increasing complexity parameter (C_p).

bullets should lead to a more or less obvious conclusion as to the location of the rosette center. To quantify this uncertainty, ten bullet rosettes are chosen at random and a bullet length analysis is performed five times on each rosette. The relative standard deviation between the tests is found to be 2.7 %.

While there is a high variation in the number of bullets that are observed from three to as high over twelve, the median is consistently between seven and eight across all temperatures of the analysis. This is only slightly higher than the four to seven mean number of bullets reported by Um et al. (2015). This discrepancy can be explained by Um et al. (2015) analyzing images from only one viewing angle, causing some bullets in the background to be obscured by those in the foreground and thus under-representing of the number of bullets. However, even with stereo imaging the complex three-dimensional nature of bullet rosettes poses complications in accurately identifying the number of bullets present on each rosette. While as a rule all bullet rosettes used for the bullet microphysical analysis have been filtered to only include rosettes where the number of bullets could confidently be stated, it is still possible for bullets in the background to be hidden by those imaged in the foreground. This

https://doi.org/10.5194/egusphere-2024-3316
Preprint. Discussion started: 4 November 2024

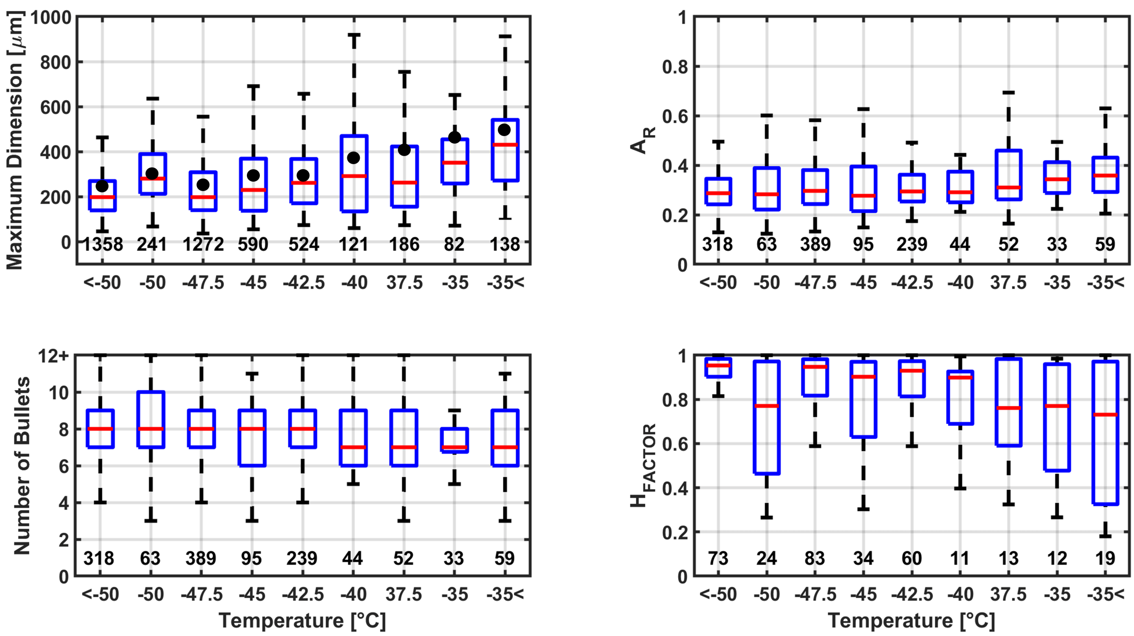

Figure 4. The bullet rosette maximum dimension (top left) for all accepted bullet rosettes with black dots to indicate median values for the 1292 rosettes accepted for a bullet analysis, and the bullet AR_B (top right), number of bullets per rosette (bottom left), and H_{FACTOR} of individual bullets (bottom right) for further manually analyzed bullet rosettes grouped by temperature (H_{FACTOR} = 1 is completely hollow). The red horizontal lines within the boxes indicate the median value for that temperature. The values above the x-axis indicate the total number of bullet rosettes for that group.

is true despite the PHIPS stereo images representing viewing angles separated by 120°. The authors find this to be particularly true for rosettes with more than six bullets; beyond twelve bullets an accurate identification of the number is nearly impossible. Thus, the median value of seven to eight bullets per rosettes found here can be under-representative to some degree.

Of the 1292 bullet rosettes chosen for a manual bullet analysis, 329 have at least one bullet which is not only hollow but has the full extent of the hollowness observable within its associated image. While the H_{FACTOR} reaches as low as 0.2, most bullets with hollowness observed have an H_{FACTOR} between 0.6 and 1.0, indicating extensive hollowness. In comparison, Schmitt and Heymsfield (2007) reported finding rosette shaped crystals with hollow bullets to have hollow components extending on average 88 $\pm$ 10 % the length of the bullet. Just as was mentioned with the calculation of the AR_B, there is some uncertainty with the determination of the location of the pixels relating to H_{FACTOR}. As is done to calculate the uncertainty bullet length, a hollowness analysis is performed five times on ten randomly selected hollow rosettes. The relative standard deviation between the tests is found to be 4.8 %. While there is a trend toward a decrease in hollowness with increasing tem-

https://doi.org/10.5194/egusphere-2024-3316
Preprint. Discussion started: 4 November 2024

perature, which disagrees with previous literature such as Bailey and Hallet (2009), the lack of statistical robustness makes this result inconclusive.

Figure 5A and Fig. 5B show bullet length L_B and W_B with respect to rosette maximum dimension D_{max}, respectively. Data point colors correspond to H_{FACTOR}, with grey squares indicating rosettes for which the degree of hollowness is unmeasurable. Both L_B and W_B have a positive correlation (R^2 = 0.94 and 0.66, respectively) with D_{max}, with L_B often a factor of three to five greater than W_B (Fig. 5C). These findings are consistent with Fridlind et al. (2016). Figure 5D shows rosette projected area (A) with respect to D_{max} with the results of Fridlind et al. (2016) and the Bucky Ball method of Um and McFarquhar (2011) included. There is strong agreement between this study and Fridlind et al. (2016) until D_{max} = 800 µm when Fridlind et al. (2016) slightly higher, in contrast to the Bucky Ball method which begins to deviate significantly at D_{max} = 600 µm. Despite the similar bullet sizes between this work and Fridlind et al. (2016), there is notable difference relating m to D_{max} (Fig. 6A). While the calculated mass in this study and that of Fridlind et al. (2016) has nearly identical trends with increasing size, the mass of Fridlind et al. (2016) is consistenly lower by as much as 35 %. This can be explained by assumptions made on the number of bullets per rosette. In this study each m is calculated using each individual rosette's determined number of bullets, where as Fridlind et al. (2016) assumes each rosette to have six bullets. As shown in Fig. 4, seven to nine bullets are often found on a single rosette. As Fridlind et al. (2016) also does not account for H_{FACTOR}, it is apparent that the number of bullets is a stronger deciding factor in m although both are necessary to accurately calculate m. The same effect can be seen in relating m to A (Fig. 6B). The parameterizations for relating both D_{max} and A can be found within their respective panel legends. Both of these effects on m become increasingly significant when applied to the rosette effective density ρ_e (Fig. 7). While rosettes with D_{max} = 1000 µm show results higher than those of Fridlind et al. (2016) by approximately 50 %, this reduces to only aproximately 10 % higher as D_{max} approaches 100 µm. For V_t the difference in mass has an even stronger effect (Fig. 8). Calculated V_t ranges from 50 to 430 $\mathrm{cm\ s^{-1}}$ for D_{max} between 100 and 900 µm; nearly two times higher than the magnitude of values reported by Fridlind et al. (2016). The difference in V_t is unsurpsing as V_t is directly dependent on both mass and the projected area. While the projected areas in both this study and Fridlind et al. (2016) are similar, the differences in mass are enough to explain the considerable discrepency in V_t. While beyond the scope of this analysis, the effect of such a difference in V_t would be interesting to explore in radiative and climate modeling applications.

3.2 Single-Scattering Properties

Figure 9 shows the measured light scattering functions with their associated g and C_p values and the respective standard deviations for all bullet rosettes with analyzable scattering functions, solid rosettes, hollow rosettes, and inclusion rosettes. Each angular scattering function is an average of indidual and presumably randomly oriented particle measurements within the categories. Solid circles indicate the PHIPS measurements from the 18° to 170° angles with 8° resolution. The solid black line and dashed colored lines show the retrieved scattering functions (without diffraction) for calculating g and C_p from the 0° to 180° angles with 0.06° resolution.

Hollow and inclusion rosettes show very similar differential scattering cross sections, with the magnitude of the inclusion rosette angular scattering function increasing only slightly from 60° to 180° relative to the scattering function of the hollow

https://doi.org/10.5194/egusphere-2024-3316
Preprint. Discussion started: 4 November 2024

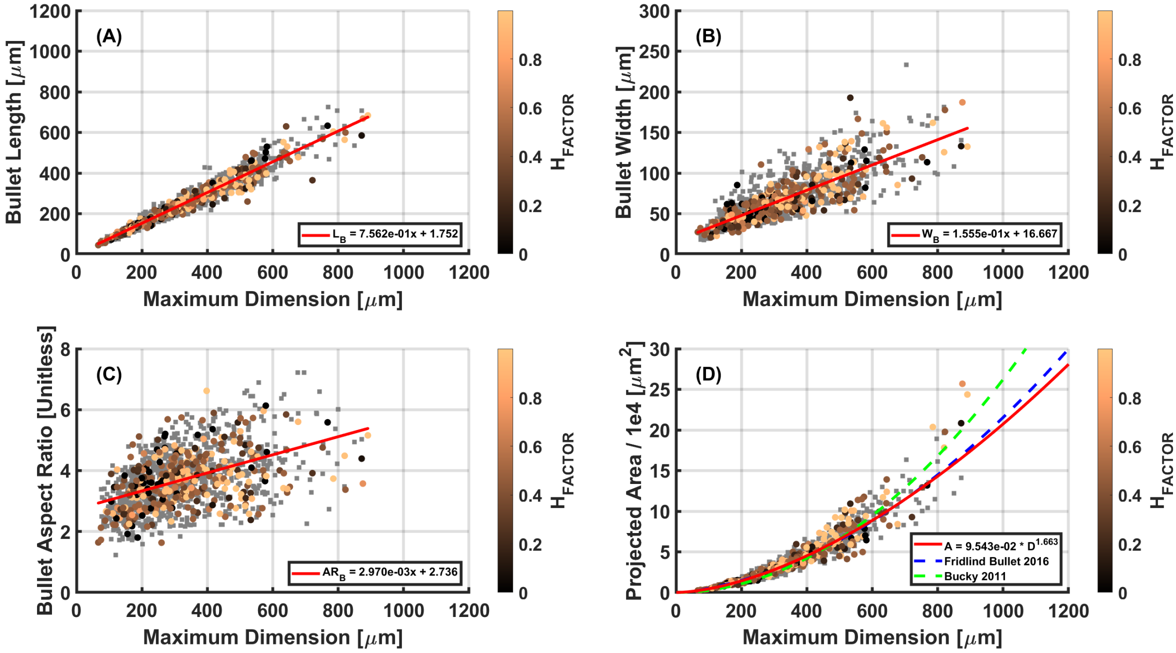

Figure 5. Bullet rosette and individual bullet microphysical properties as related to bullet rosette maximum dimension, color coded by the corresponding H_{FACTOR}. Rosettes for which the degree of hollowness is unmeasurable are indicated with a grey square.

rosettes; however, the magnitude of the solid bullet rosettes in the 60° to 80° range has a peak which is not shared with either hollow or inclusion rosettes. This is followed by a shift toward the backward direction in the 120° to 140° dip and the 140° to 170° peak of the solid rosettes. It should be noted that the number of solid rosettes is significantly lower (33) than rosettes with degrees of hollowness (572) or air inclusions (144), and thus the mean differential cross section is statistically less robust, and an assumption of orientation averaged population is likely not valid as specular reflections of individual particles could have a large affect on the result.

PHIPS measurements of each rosette category show a fairly smooth behavior from 0° to 60°. This is in strong contrast to previous modeled results which show rapid drops from the forward most angles followed by several peaks primarily corresponding to the 22° and 46° halos. Note that both 22° and 46° are between PHIPS measurement angles. Schmitt et al. (2006) Fig. 3 shows theoretical ray-tracing scattering phase functions for both solid and hollow bullet rosettes that assume six bullets, a semi-randomized orientation, AR_B of 0.25, pristine surfaces, and a H_{FACTOR} of 1.0 for the hollow bullet rosette. While the results of Schmitt et al. (2006) show several peaks in angles less than 50° for both the simulated solid and hollow rosettes, these features are entirely missing in the scattering functions obtained by the PHIPS. This contrast is even more pronounced between the solid rosettes and this result can also be seen in Iaquinta et al. (1995). This can be attributed to the theoretical

https://doi.org/10.5194/egusphere-2024-3316
Preprint. Discussion started: 4 November 2024

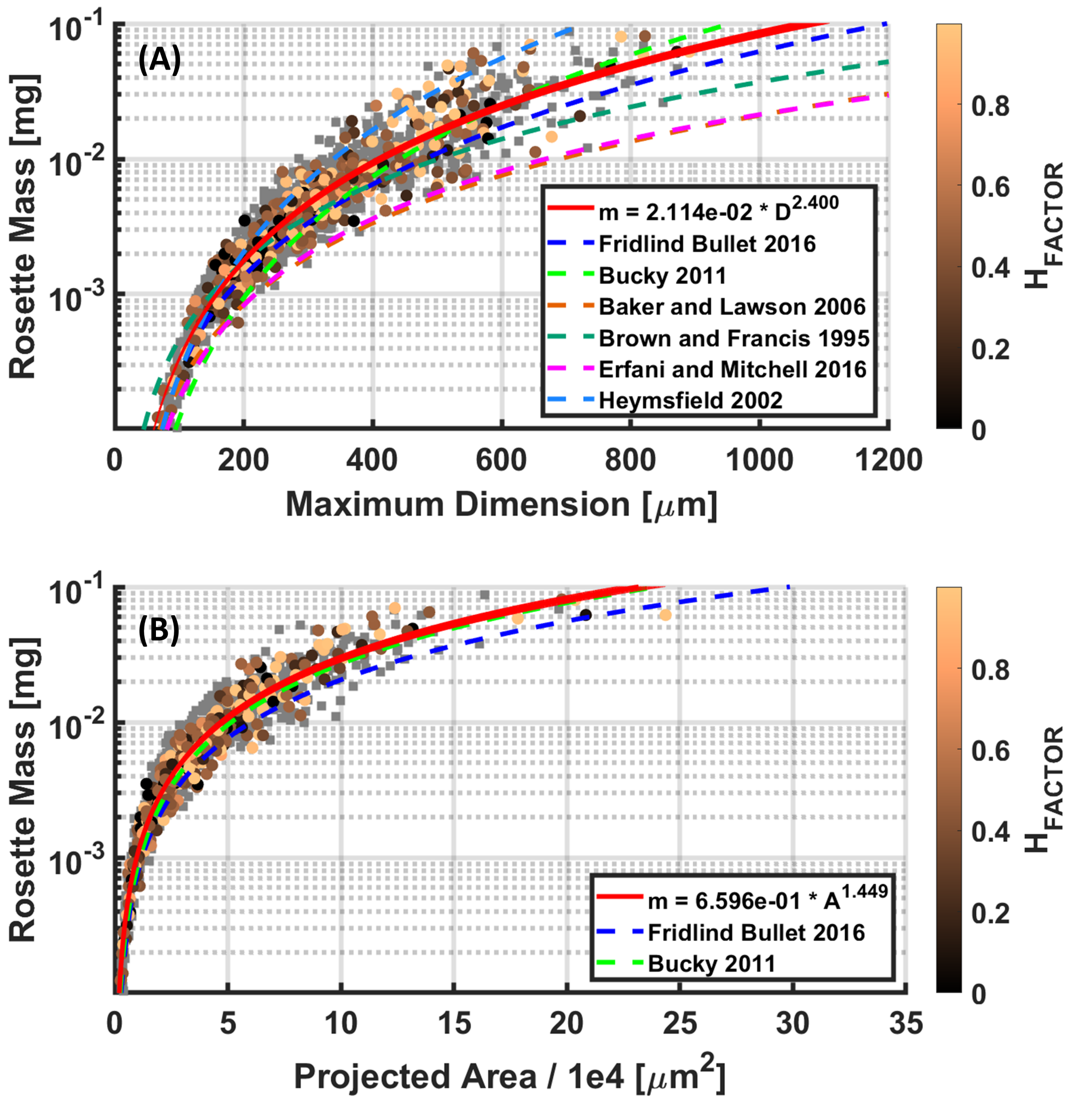

Figure 6. Bullet rosette maximum dimension and projected area (*A*) as related to bullet rosette mass, color coded by the corresponding H_{FACTOR}. Rosettes for which the degree of hollowness is unmeasurable are indicated with a grey square.

simulations applying idealized pristine surfaces rather than accounting for crystal complexity. This will be discussed further in the following paragraphs.

In the sideward and backward direction, the results of Schmitt et al. (2006) and Iaquinta et al. (1995) are quite similar; however, there are further differences when compared with the in situ measured values. Theoretical results show a general flattening of the scattering functions of both solid and hollow rosettes in the sideward directions. In all categories of the PHIPS measured bullet rosettes there is a continued decrease in the scattering function until approximately 130° when the trend

https://doi.org/10.5194/egusphere-2024-3316
Preprint. Discussion started: 4 November 2024

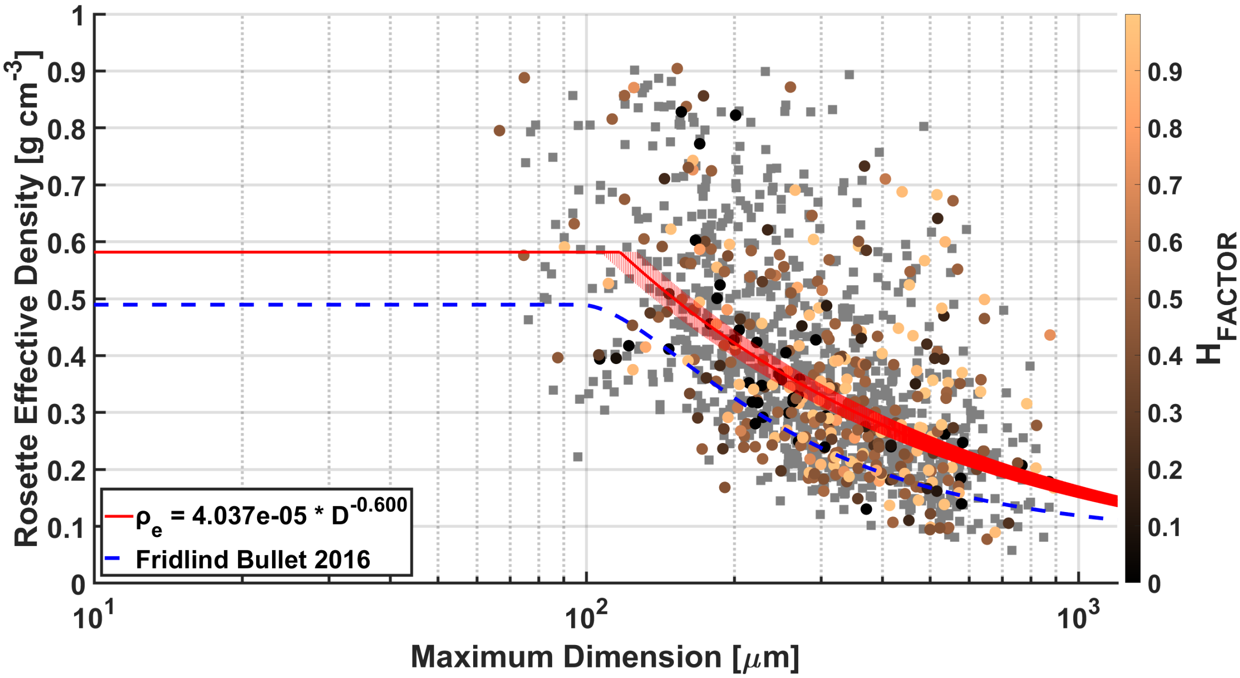

Figure 7. Bullet rosette effecteive density as related to the rosette maximum dimension, color coded by the correspondingH_{FACTOR}. Rosettes for which the degree of hollowness is unmeasurable are indicated with a grey square. To account for the natural limit of ice density, values of the effective density parameterization for D_{max} = < 150 µm are limited to the calculated mean effective density of the smallest observed roesttes.

reverses and a local maximum is reached for all rosettes, hollow rosettes, and inclusion rosettes at 145°. For solid rosettes these features are shifted to 135° and at 155°, respectively. While this local maximum, sometimes refered to as "ice bow", is readily apparent in Iaquinta et al. (1995), no such fluctuation exists in the sideward directions of Schmitt et al. (2006).

PHIPS retrieved g values between each category of bullet rosette show an absolute maximum difference of 0.029 (a factor of five larger than the uncertainty) between the lowest values (g = 0.692 for inclusion rosettes) and the highest values (g = 0.721 for hollow rosettes). When accounting for the uncertainty of 0.006 (more information in Appendix A), this results in a maximum percent difference of 5.8 % between categories. As C_p tends to negatively correlate with positive values of g, the lowest value is 0.498 (hollow rosettes) and the highest value is 0.562 (inclusion rosettes). At an absolute maximum difference of 0.064, there is a maximum percent difference of 16.9 % between categories. While it is evident that the type (solid, hollow, or inlcusion) of rosette has little impact on g or C_p, other physical properties require consideration. The next critical point of analysis is to relate g and C_p to bullet rosette size.

Figure 10 shows g versus C_p for all bullet rosettes according to their respective area equivalent diameter (D) as measured by PHIPS images, grouped by five bin mean sizes: 60, 80, 125, 175 and 225 µm. Each D is equal to the diameter of a sphere

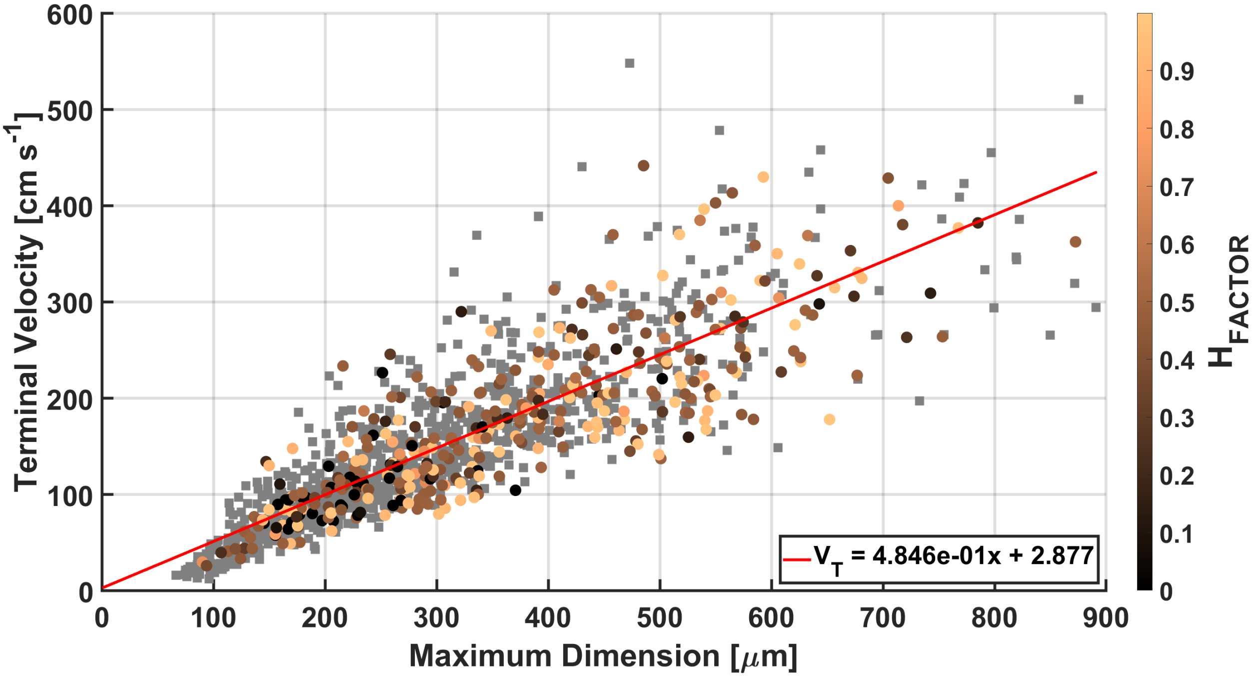

Figure 8. Bullet rosette terminal velocities as related to the rosette maximum dimension, color coded by the correspondingH_{FACTOR}. Rosettes for which the degree of hollowness is unmeasurable are indicated with a grey square.

having the same projected area as the corresponding measured rosettes. The mean angular scattering function for the bullet rosettes is calculated for each size group, and that mean scattering function is used to retrieve one g and one C_p value for the group. It is assumed that the populations within these groupings are orientation averaged. Excluding the largest 225 µm bin, there is a strong linear negative correlation between g and D. Values for g range from 0.700 at D = 175 µm to 0.751 at D = 60 µm, with C_p having a strong linear negative correlation spanning from 0.470 to 0.542. Deviation from the trend of reducing g with inceasing D at the largest size has not yet been determined. As Iaquinta et al. (1995) reported theoretical g values ranging from 0.788 to 0.876 for solid rosettes, and Schmitt et al. (2006) reported a range from approximately 0.800 to 0.845 for hollow rosettes, there is an approximately 13.6 $\%$ mean difference between the now measured g and previous theoretical calculations. This difference can be explored by introducing previously omittied surface roughness into new ray-tracing simulations.

The shaded areas of Fig. 10 indicate the range from minimum to maximum theoretical g by varying simulated roughness parameters (δ and σ^2) of the ray-tracing simulations for solid and hollow rosettes with the same D bins as those of the PHIPS. The assumed rosette geometry is discussed in section 2.2. Additionally, the hollow bullet rosettes have an H_{FACTOR} of 0.9 applied (seen within Fig. 10). With little to no simulated roughness applied (when C_p < 0.45), the modeled values of g are similar to those of both Iaquinta et al. (1995) and Schmitt et al. (2006). However, when the simulated surface roughness is increased (when C_p > 0.45), g values gradually reduce until the ray-tracing results of solid rosettes match the observed g

https://doi.org/10.5194/egusphere-2024-3316
Preprint. Discussion started: 4 November 2024

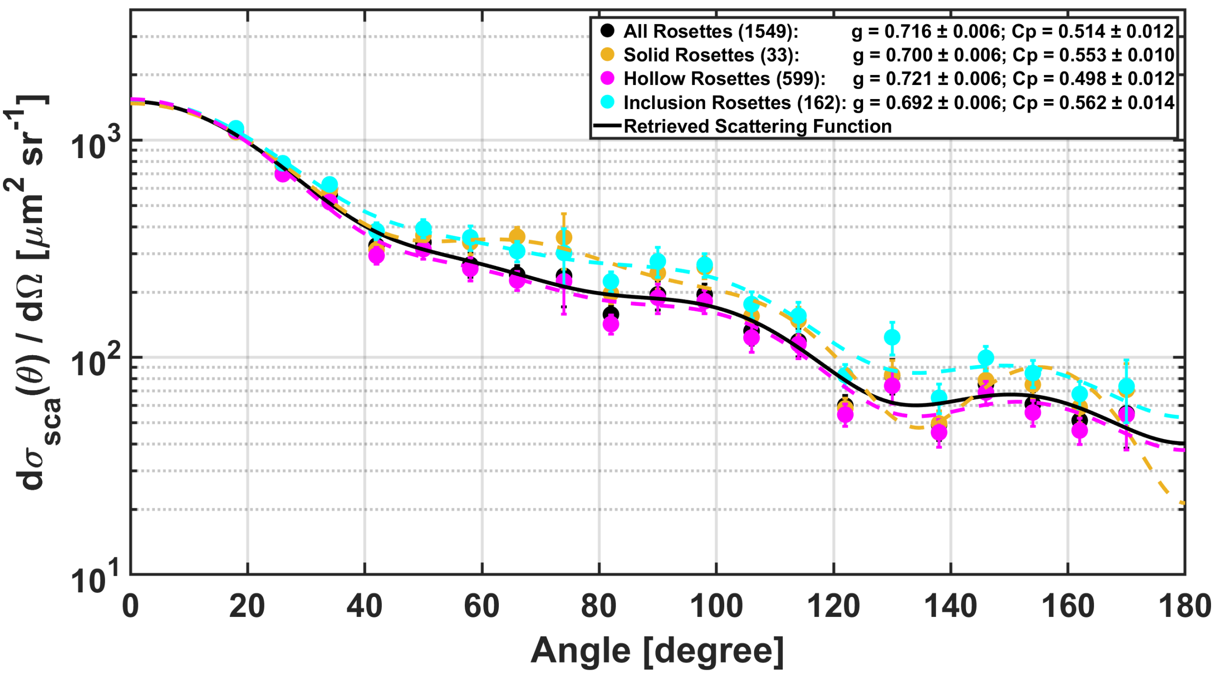

Figure 9. The mean bullet rosette differential scattering cross sections with their associated asymmetry (g) and complexity (C_p) parameters and the respective standard deviations separated by bullet rosette category. The values in parentheses indicate the number of rosettes per category. The solid black line and the dashed colored lines show the retrieved scattering function used to calculate g and C_p. The vertical lines indicate measurement uncertainty.

values. As can be seen in Table 1, representing the observed in situ data requires a signficant amount of simulated roughness (δ or $\sigma^2 > 0.6$). Similar observations have been shown by Järvinen et al. (2018), and similar simulated results have been found by Baum et al. (2010), Yang et al. (2013), Tang et al. (2017) and others. Interestingly, while increasing the complexity of the simulated hollow rosettes reduces their g values, it does not do so enough to fit the measurements within the bounds of uncertainty.

Iaquinta et al. (1995) suggested that bullet rosettes can be represented using simpler models of columns. Such an ability is desirable as simulations for columns can be completed in shorter times, utilizing less computational resources. Figure 10 also shows simulated g and C_p values for solid columns using both the UTA and GTA methods. The UTA results fit the measured bullet rosette g and C_p values quite well, nearly perfectly overlapping those of the simulated solid rosettes. Although the GTA method has a reputation for more sophisticatedly simulating ice crystal complexity, the UTA method produces values that are significantly more representative of the PHIPS measurements. To fit within the bounds of uncertainty for even half of the in situ data points, an MFP of 300 is required for the GTA method, with sensitivity tests (unshown) indicating that higher MFP values generate further unrealistic trends.

https://doi.org/10.5194/egusphere-2024-3316
Preprint. Discussion started: 4 November 2024

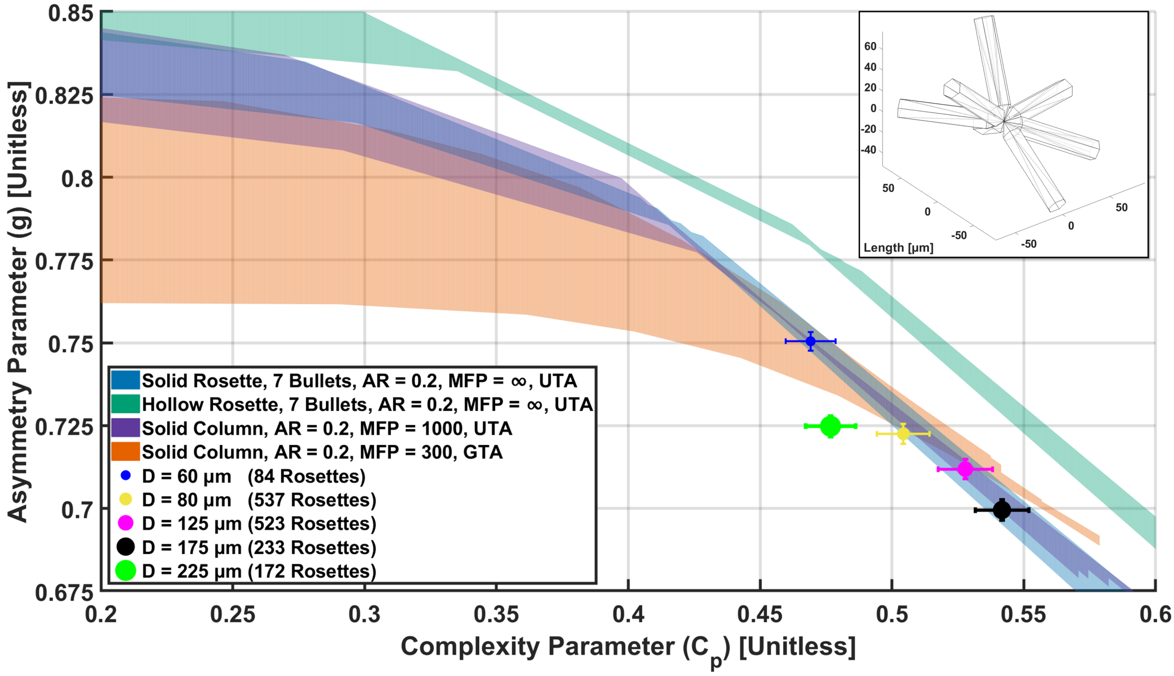

Figure 10. Bullet rosette asymmetry parameters (g) and their corresponding complexity parameters (C_p) separated by area equivalent diameter(D) as measured by the Particle Habit Imaging and Polar Scattering (PHIPS) probe. The values in parentheses indicate the number of rosettes per size bin. Shaded areas show the range from minimum to maximum theoretical results of ray-tracing simulations for solid rosettes, hollow rosettes, and columns. An example modeled hollow rosette can be seen in the upper right, which corresponds to a D of 125 µm.

Table 1. The distortion parameter (δ) and complexity parameter (σ^2) resulting in the closest match to the ray-tracing simulated asymmetry parameter (g) for solid bullet rosettes, hollow bullet rosettes, and solid columns with the corresponding in situ measured g by area equivalent diameter (D). UTA Solid and hollow rosettes have a have a mean free path (MFP) of infinity. UTA and GTA solid columns have a MFP of 1000 µm and 300 µm. UTA have (δ) ranging from 0.0 to 0.9 increasing by 0.3. GTA have a σ^2 range of 0.1 to 0.9, increasing by 0.1.

Bin Mean Diameter	UTA Solid Rosettes	UTA Hollow Rosettes	UTA Solid Columns	GTA Solid Columns
D [µm]	δ	δ	δ	σ^2
60	0.70	0.68	0.72	0.75
80	0.77	0.73	0.79	0.86
125	0.79	0.74	0.80	0.86
175	0.81	0.76	0.83	0.86
225	0.74	0.70	0.74	0.66

https://doi.org/10.5194/egusphere-2024-3316
Preprint. Discussion started: 4 November 2024

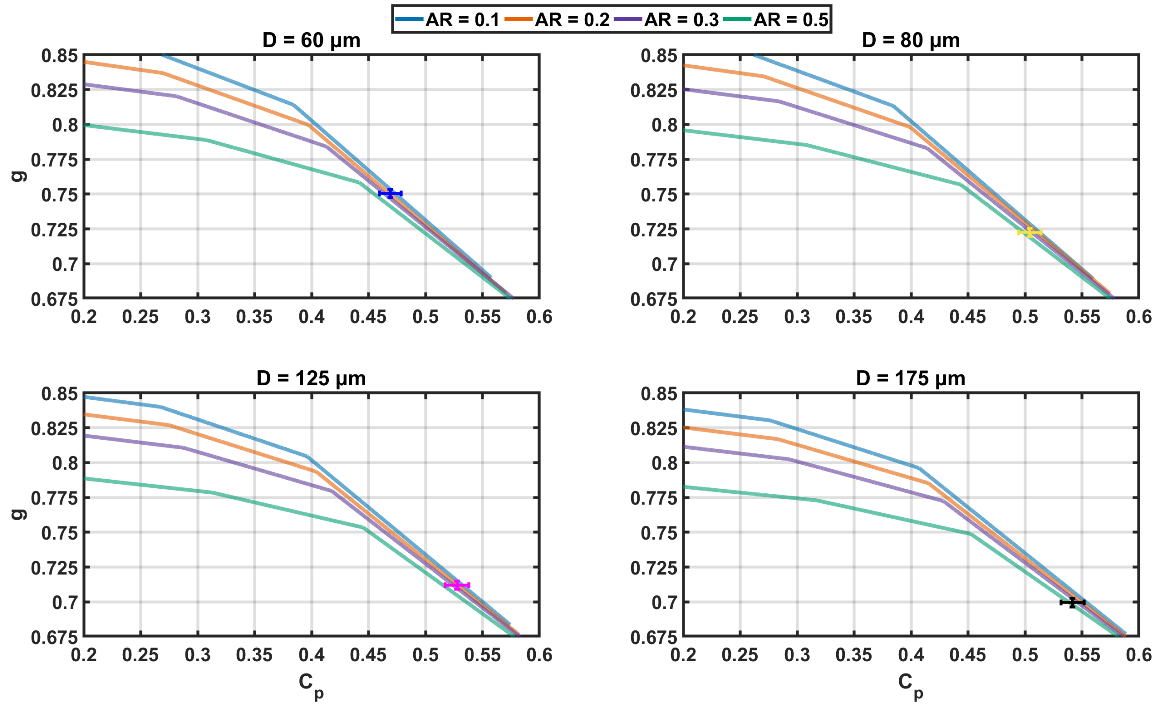

Figure 11. The theoretical results of ray-tracing simulations for solid columns with varying aspect ratios (AR) using the uniform tilted angle distrubtion method (UTA) for area equivalent diameters (D) ranging from 60 µm to 175 µm compared to the Particle Habit Imaging and Polar Scattering (PHIPS) probe bullet rosette measurments of equal size.

While the UTA simulation results lend credence to the claim that bullet rosette models can be replaced with those of columns, Iaquinta et al. (1995) also stated that the AR of the modeled columns would need to match that of AR_B for a proper substitution. Figure 11 shows the same PHIPS measured results as in Fig. 10, but in relation to theoretical results of ray-tracing simulations for solid columns using the UTA method with AR of 0.1, 0.2, 0.3, and 0.5. With little to no simulated roughness ($C_\mathrm{p} < 0.45$), the difference between simulations is significant. However, with increasing levels of simulated rougness the spread between results narrows. With $C_\mathrm{p} > 0.45$, the largest differences occure in the range of $g = 0.75$ to $g = 0.77$, where there is a maximum percent difference of only 2.2 % between an AR of 0.1 and 0.5. For each of the measured rosette size bins the calculations are well within uncertainty, indicating that with sufficent complexity the relationship between AR_B and the AR of the simulated column is not a critical factor.

Our observations highlight that the largest effect on the g (C_p) values of bullet rosettes is caused by small scale morphological complexity that is likely comprised of nano-scale surface roughness, stepped patterns within hollow cavities (stepped hollowness), internal inclusions, and/or other deformations rather than micro-scale properties such as D_{max}, number of bullets, bullet geometry and AR_B. Some evidence of crystal complexity can be clearly seen in Figs. 1 and 3 as a black shading in the stereo-microscopic images; the complexity causes an increase in light diffusion as there is a decease in the amount of light

https://doi.org/10.5194/egusphere-2024-3316
Preprint. Discussion started: 4 November 2024

which can travel undisturbed. These results showcase the necessity of a (single particle) polar nephelometer such as the PHIPS to bridge the gap between numerical simulations and direct measurements of atmospheric crystals.

4 Summary and Conclusions

Bullet rosettes commonly occur in high altitude cirrus clouds, and thus play an important role in the radiative budget of the Earth. To properly model and account for the extent of the radiative effect from bullet rosettes, one must understand their single-scattering properties. In this study we have examined both the microphysical and single scattering properties and their link of real atmospheric bullet rosettes measured by the PHIPS during the CIRRUS-HL airborne campaign. Both the microphysical and single scattering properties were measured on the same individual crystals. We have shown that a cirrus cloud during CIRRUS-HL of temperatures at or below -50 °C is comprised of bullet rosettes on average between 10 and 20 $\%$. The median maximum dimensions were between 200 μm and 420 μm with the largest median maximum dimensions observed at -35 °C and warmer, the median number of bullets between seven and eight, and a me at temperatures above -35 °C, and which primarily increased with decreasing temperature to values as high as 1.0. Updated parameterizations for relating rosette maximum dimension to rosette mass, effective density and terminal velocity, as well as the rosette projected area to mass are given, highlighting the importance of accounting for both the number of bullets per rosette as well as the degree of bullett hollowness.

Asymmetry parameters for all rosettes was found to be 0.718, with little difference between solid (g = 0.700), hollow (g = 0.721) and inlcusion (g = 0.692) rosettes, with each case lower than previously suggested g based on simulations using rosettes with idealized pristine surfaces. For all rosettes grouped by similar area equivalent diameters (D), g was found to decrease with size and range from as low as 0.700 to as high as 0.751, which is lower than previous theoretical studies with a mean percent difference of 13.6 $\%$. The primary cause of the difference between theoretical and actual bullet rosette g values was shown to result from surface level and internal complexity (e.g. surface roughness, stepped hollowness) rather than the microphysical properties (e.g. D_{max}, number of bullets, bullet geometry and bullet aspect ratio AR_B). This complexity renders assumptions in ray-tracing models that bullet rosettes have idealized pristine surfaces unrealistic, causing the discrepancy between the g values found herein and the results of previous theoretical studies. It should also be noted that while the ray-tracing simulations of hollow bullet rosettes were found to be outside the bounds of uncertainty of the in situ measured rosettes, the ray-tracing simulations of solid columns and bullet rosettes were within. This supports previous claims that bullet rosettes can be represented with a columnar model, though only if it appropriately accounts for crystal complexity with little importance on the column AR. Suggestions of representative values for crystal complexity simulating parameters are included relative to D for each of the modeled habits. Work is needed to gauge the full effect of discrepancies between theoretical transfer simulations and measured results of bullet rosette single-scattering properties in radiative transfer simulations, though lower g values in the short wave lead to more reflected short wave radiation.

While radiative transfer simulations are beyond the scope of this paper, Järvinen et al. (2018) has shown that increased cloud ice crystal complexity (ice crystal g = 0.75) has a significant global climate cooling effect. Therefore, a reduction in g from cloud in situ bullet rosettes caused by crystal complexity, compared to higher g values of previous theoretical studies

https://doi.org/10.5194/egusphere-2024-3316
Preprint. Discussion started: 4 November 2024

that assumed idealized pristine surfaces, must be accounted for going forward with climatological and radiative modeling to achieve accurate results.

385 *Data availability.* Bullet rosette data from the PHIPS probe is available in KITopen. Alll processed PHIPS data from CIRRUS-HL, and the atmospheric state data, can be accesed from the HALO database (https://halo-db.pa.op.dlr.de/mission/125).

Appendix A: PHIPS Data Correction and Uncertainty

One significant factor contributing to uncertainties in retrieving g and C_p is the non-uniform response of the scattering channels to light scattering signals of the same intensity. This non-uniform response can be attributed to potential differences in the
390 coupling of the scattered light to the optical fibers, variations in signal transmission within the optical fibers, dissimilarities in how light is transmitted from fibers to the multi-anode photomultiplier tube (MAPMT), and by the channel-to-channel variation of the anode sensitivity within the MAPMT. This non-uniform response of the scattering channels can be better understood and collectively characterized by measuring particles with a known phase function. For example, using spherical particles with a known size and refractive index.

395 PHIPS was calibrated during CIRRUS-HL with 81 polystyrene microspheres (Thermofisher, 2024) having diameters of 20 μm and a refractive index of 1.605 + 0.0003i at a wavelength of 532 nm (Jones et al., 2013). Using the size and refractive index, a theoretical phase function was calculated using the Lorenz-Mie theory (Mie, 1908) with an angular resolution of 0.09°. The phase function was then integrated over the solid angles of the PHIPS scattering channels to cacluate the expected scattered power per detection angle in nW. Once integrated, a recursive function determines a scaling factor for each microsphere
400 to convert the PHIPS measured counts to nW by minimizing the square residuals per scattering angle between the PHIPS measurements and theoretical calculation. With the conversion factor applied to the PHIPS results, the ratio of the theoretical function to the PHIPS measured function was calculated by channel to quantify the non-uniformity of the PHIPS response and generate channel specific correction factors. Uncertainty in the MAPMT measurements combined with imperfections in the sphericity and size of the microspheres results in a variability of correction factors, and thus the median and standard deviation
405 is taken for each channel.

Figure A1 shows the measured angular scattering function of all 81 polystyrene microspheres and the theoretical phase function. The blue dashed line is the initial, uncorrected scattering function of a randomly selected microsphere. The red dashed line is the theoretical Lorenz-Mie function calculated using the sphere's size and refractive index. The green line is the resulting PHIPS scattering function after the multiplicative factors were applied to the measurements of each of the scattering
410 channels. The bottom of Fig. A1 shows the resulting residuals. While the 18 - 162° scattering intensities as measured by the PHIPS match that of the theoretical Lorenz-Mie function for the 20 μm spheres quite well, the Lorenz-Mie function is approximately 1.8 times as intense at the 170° angle. Sensitivity tests on how minor changes of the refractive index affect the resulting Lorenz-Mie calculation (not shown) indicate that the backward angles are the most sensitive to refractive index

https://doi.org/10.5194/egusphere-2024-3316
Preprint. Discussion started: 4 November 2024

variations. Variations in the index of refraction combined with imperfections in the microsphere sphericities and surfaces, as well as geometrical scattering effects due to the Gaussian profile of the laser beam, may be the cause of the discrepency. For further discussions on PHIPS scattering measurements as shown with polystyrene microspheres, piezo generated droplets, and atmospheric ice crystals, see Schnaiter et al. (2018).

Since the discrepency between PHIPS measurements and the theoretical calculation occurs only in the backward direction, and g is most affected by scattering in the forward direction, correction factors are only applied to angles 18 - 66° where there is no uncertainty caused by deviations in the sphericity. However, even without a correction applied to data, the standard deviation in the calculated channel correction factors can still be used as an estimate in the channel uncertainty and thus the uncertainty in the g and C_p calculations. While not shown, a sensitivity test in which corretion factors were applied to channels 18 - 170° was conducted, and the effect on g was found to be only 0.07 %, making the occlusion of any correction to angles 74 - 170° negligable. The correction factors and their standard deviations for each channel as applied to the CIRRUS-HL data can be found in Table A1.

Appendix B: Bullet Volume Equations

Calculating bullet rosette mass requires the mean bullet volume ($\overline{V_B}$) per rosette. By treating the bullets as hexagonal columns with hexacone caps and accounting for hollowness when applicable, ($\overline{V_B}$) can be calculated using:

$$\overline{V_B} = 3ab(\overline{L_B} - \overline{L_{HC}}) + \sqrt{3}\frac{a^2\overline{L_{HC}}}{2} - \sqrt{3}\frac{a^2\overline{H_{FACTOR}L_B}}{2}, \tag{B1}$$

where a is the length of a hexagonal edge, b is the length to the center of a hexagon from the center of the hexagonal edge, and $\overline{L_{HC}}$ is the hexacone height. Using the basic geometry of a hexagone, a is calculated as:

$$a = \frac{\overline{W_B}}{tan(60)}, \tag{B2}$$

and b is calculated as:

$$b = \frac{\overline{W_B}}{2}. \tag{B3}$$

As the bullet rosette caps are often difficult to discern in images containing rosettes with high numbers of bullets, L_{HC} is not dirrectly measured. Instead, this study assumed both an L_{HC} that is 5 % and 20 % of L_B to account for a range of reasonable bullet cap lengths.

To account for length and width errors resulting from L_B and W_B being assesed from bullet rosette projections on 2-D images, a simulated rosette projection with known L_B and W_B is generated with ten random orientations. The L_B and W_B is then calculated manually for comparison to the known values. It is found that L_B tends to be underestimated by 15 % and W_B tends to be underestimated by 0.007 %. The L_B and W_B measured from the 2-D projections are adjusted by adding the 15 % and 0.007 % respectively.

https://doi.org/10.5194/egusphere-2024-3316
Preprint. Discussion started: 4 November 2024

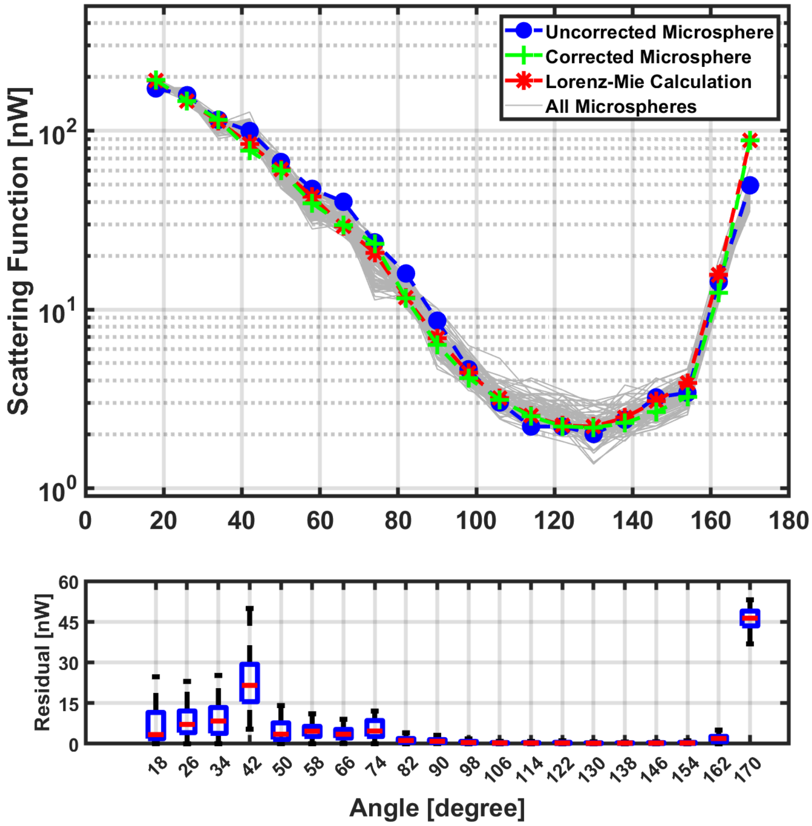

Figure A1. An example of one of the 81 microspheres used for the calibration measurements taken by the Particle Habit Imaging and Polar Scattering (PHIPS) probe during the Cirrus in High Latitudes (CIRRUS-HL) airborne campaign (top). Angles measured by the PHIPS (18 - 170°) are corrected using a fit to the theoretical Lorenz-Mie curve. The calculated residuals between the theoretical Lorenz-Mie calculation and the corrected PHIPS channels for each of the 81 microspheres are inclucded (bottom). Only corection factors for angles 18 - 66° are applied to the CIRRUS-HL data.

Appendix C: Rosette Terminal Velocity Equations

Calculating bullet rosette terminal velocity (V_t) requires the derivation of air density (ρ_a) and the drag coefficient C_D. ρ_a can be calculated using the well known equation:

$$\rho_a = \frac{P}{R_{specific}T}. \tag{C1}$$

where P is the atmospheric pressure in Pa, $R_{specific}$ is the specfic gas constant for dry air (287.05 j kg^{-1} K^{-1}), and T is the temperature in K. Following Mitchell (1996), C_D can be calculated as:

$$C_D = C_0\left(1 + \frac{D_0}{R_e^{\frac{1}{2}}}\right)^2, \tag{C2}$$

https://doi.org/10.5194/egusphere-2024-3316
Preprint. Discussion started: 4 November 2024

Table A1. The Particle Habit Imaging and Polar Scattering (PHIPS) scattering data correction factors and their standard deviations as applied to the Cirrus in High Latitudes (CIRRUS-HL) airborne campaign data.

Scattering Angle	Correction Factor	Standard Deviation
18	1.0326	0.0472
26	0.9452	0.0391
34	1.0859	0.0723
42	0.7767	0.0671
50	1.0348	0.1043
58	1.0723	0.1352
66	0.9055	0.0950
74	1.0	0.2875
82	1.0	0.1043
90	1.0	0.1584
98	1.0	0.1204
106	1.0	0.1449
114	1.0	0.1516
122	1.0	0.1179
130	1.0	0.1756
138	1.0	0.1503
146	1.0	0.1303
154	1.0	0.1396
162	1.0	0.1440
170	1.0	0.3183

where C_0= 0.292 and D_0 = 9.06 are both constants for rigid spheres (Abraham, 1970), and R_e is the Reynolds number:

$$R_e = \frac{{D_0}^2}{4}\left[\left(1+\frac{4X^{\frac{1}{2}}}{{D_0}^2{C_0}^{\frac{1}{2}}}\right)-1\right]^2. \tag{C3}$$

X is the Best number and is calculated as:

$$X = \frac{2mg_c\rho_a{D_{max}}^2}{A\eta^2}, \tag{C4}$$

where η is the dynamic viscosity of air and can be calculated using the Sutherland-law (White, 2005):

$$\eta = \eta_0\left(\frac{T}{273}\right)^{\frac{3}{2}}\left(\frac{273+111}{T+111}\right). \tag{C5}$$

η_0 is a constant $1.716e^{-5}$ $\mathrm{N\,s\,m^{-2}}$.

Author contributions. This bullet rosette study was conceptualized by SWW and EJ. SWW conducted data analysis and led the manuscript writing. MS developed the PHIPS, provided insight into measurement interpretation, and conducted data analysis. SWW, EJ, and MS collected the measurments during CIRRUS-HL. GX provided the code and expertise necessary for the ray-tracing analysis. FN supplied image analysis ice crystal habit identification. EJ provided funding and guidance in analyzing cirrus cloud data and asymmetry parameters, conducted data analysis, and provided general insight. All authors have reviewed, commented on, and approved the manuscript.

Competing interests. Martin Schnaiter and Emma Järvinen are members of schnaiTEC GmbH, the PHIPS manufacturer. Martin Schnaiter is employed part-time by schnaiTEC GmbH.

Acknowledgements. We would like to thank the members of the CIRRUS-HL field operations for their efforts in acquiring the data utilized herein. This work was funded by the Helmholtz Association's Initiative and Networking Fund (grant agreement no. VH-NG-1531), the Helmholtz Association research porgam "Atmosphere and Climate".

https://doi.org/10.5194/egusphere-2024-3316
Preprint. Discussion started: 4 November 2024

References

Abdelmonem, A., Järvinen, E., Duft, D., Hirst, E., Vogt, S., Leisner, T., and Schnaiter, M.: PHIPS–HALO: the airborne Particle Habit Imaging and Polar Scattering probe – Part 1: Design and operation, Atmospheric Measurement Techniques, 9, 3131–3144, https://doi.org/10.5194/amt-9-3131-2016, 2016.

Abraham, F. F.: Functional Dependence of Drag Coefficient of a Sphere on Reynolds Number, The Physics of Fluids, 13, 2194–2195, https://doi.org/10.1063/1.1693218, 1970.

Bailey, M. P. and Hallett, J.: A Comprehensive Habit Diagram for Atmospheric Ice Crystals: Confirmation from the Laboratory, AIRS II, and Other Field Studies, J. Atmos. Sci., 66, 2888–2899, https://doi.org/10.1175/2009JAS2883.1, 2009.

Baker, B. and Lawson, R. P.: Improvement in Determination of Ice Water Content from Two-Dimensional Particle Imagery. Part I: Image-to-Mass Relationships, Journal of Applied Meteorology and Climatology, 45, 1282–1290, https://doi.org/10.1175/JAM2398.1, 2006.

Brown, P. R. A. and Francis, P. N.: Improved Measurements of the Ice Water Content in Cirrus Using a Total-Water Probe, Journal of Atmospheric and Oceanic Technology, 12, 410–414, https://doi.org/10.1175/1520-0426(1995)012<0410:IMOTIW>2.0.CO;2, 1995.

Baum, B. A., Yang, P., Hu, Y.-X., and Feng, Q.: The impact of ice particle roughness on the scattering phase matrix, Journal of Quantitative Spectroscopy and Radiative Transfer, 111, 2534–2549, https://doi.org/10.1016/j.jqsrt.2010.07.008, 2010.

DLR: CIRRUS-HL – HALO Database – The High Altitude and LOng Range Research Aircraft Database: https://halo-db.pa.op.dlr.de/mission/125, last access: 17 October 2024.

Erfani, E. and Mitchell, D. L.: Developing and bounding ice particle mass- and area-dimension expressions for use in atmospheric models and remote sensing, Atmospheric Chemistry and Physics, 16, 4379–4400, https://doi.org/10.5194/acp-16-4379-2016, 2016.

Fridlind, A. M., Atlas, R., van Diedenhoven, B., Um, J., McFarquhar, G. M., Ackerman, A. S., Moyer, E. J., and Lawson, R. P.: Derivation of physical and optical properties of mid-latitude cirrus ice crystals for a size-resolved cloud microphysics model, Atmospheric Chemistry and Physics, 16, 7251–7283, https://doi.org/10.5194/acp-16-7251-2016, 2016.

Heymsfield, A. J. and Iaquinta, J.: Cirrus Crystal Terminal Velocities, Journal of the Atmospheric Sciences, 57, 916–938, https://doi.org/10.1175/1520-0469(2000)057<0916:CCTV>2.0.CO;2, 2000.

Heymsfield, A. J., Lewis, S., Bansemer, A., Iaquinta, J., Miloshevich, L. M., Kajikawa, M., Twohy, C., and Poellot, M. R.: A General Approach for Deriving the Properties of Cirrus and Stratiform Ice Cloud Particles, Journal of the Atmospheric Sciences, 59, 3–29, https://doi.org/10.1175/1520-0469(2002)059<0003:AGAFDT>2.0.CO;2, 2002.

Iaquinta, J., Isaka, H., and Personne, P.: Scattering Phase Function of Bullet Rosette Ice Crystals, Journal of the Atmospheric Sciences, 52, 1401–1413, https://doi.org/10.1175/1520-0469(1995)052<1401:SPFOBR>2.0.CO;2, 1995.

Järvinen, E., Jourdan, O., Neubauer, D., Yao, B., Liu, C., Andreae, M., Lohmann, U., Wendisch, M., Mcfarquhar, G., Leisner, T., and Schnaiter, M.: Additional Global Climate Cooling by Clouds due to Ice Crystal Complexity, Atmospheric Chemistry and Physics Discussions, 1–24, https://doi.org/10.5194/acp-2018-491, 2018.

H. Jones, S., D. King, M., and D. Ward, A.: Determining the unique refractive index properties of solid polystyrene aerosol using broadband Mie scattering from optically trapped beads, Physical Chemistry Chemical Physics, 15, 20735–20741, https://doi.org/10.1039/C3CP53498G, 2013.

Krämer, M., Rolf, C., Luebke, A., Afchine, A., Spelten, N., Costa, A., Meyer, J., Zöger, M., Smith, J., Herman, R. L., Buchholz, B., Ebert, V., Baumgardner, D., Borrmann, S., Klingebiel, M., and Avallone, L.: A microphysics guide to cirrus clouds – Part 1: Cirrus types, Atmospheric Chemistry and Physics, 16, 3463–3483, https://doi.org/10.5194/acp-16-3463-2016, 2016.

https://doi.org/10.5194/egusphere-2024-3316
Preprint. Discussion started: 4 November 2024

Lawson, R. P., Baker, B. A., Zmarzly, P., O'Connor, D., Mo, Q., Gayet, J.-F., and Shcherbakov, V.: Microphysical and Optical Properties of Atmospheric Ice Crystals at South Pole Station, Journal of Applied Meteorology and Climatology, 45, 1505–1524, https://doi.org/10.1175/JAM2421.1, 2006.

Lawson, R. P., Jensen, E., Mitchell, D. L., Baker, B., Mo, Q., and Pilson, B.: Microphysical and radiative properties of tropical clouds investigated in TC4 and NAMMA, Journal of Geophysical Research: Atmospheres, 115, https://doi.org/10.1029/2009JD013017, 2010.

Lawson, R. P., Woods, S., Jensen, E., Erfani, E., Gurganus, C., Gallagher, M., Connolly, P., Whiteway, J., Baran, A. J., May, P., Heymsfield, A., Schmitt, C. G., McFarquhar, G., Um, J., Protat, A., Bailey, M., Lance, S., Muehlbauer, A., Stith, J., Korolev, A., Toon, O. B., and Krämer, M.: A Review of Ice Particle Shapes in Cirrus formed In Situ and in Anvils, Journal of Geophysical Research: Atmospheres, 124, 10049–10090, https://doi.org/10.1029/2018JD030122, 2019.

Liou, K.-N.: Influence of Cirrus Clouds on Weather and Climate Processes: A Global Perspective, Monthly Weather Review, 114, 1167–1199, https://doi.org/10.1175/1520-0493(1986)114<1167:IOCCOW>2.0.CO;2, 1986.

Liou, K. N., Yang, P., Takano, Y., Sassen, K., Charlock, T., and Arnott, W.: On the radiative properties of contrail cirrus, Geophysical Research Letters, 25, 1161–1164, https://doi.org/10.1029/97GL03508, 1998.

Liu, C., Lee Panetta, R., and Yang, P.: The effects of surface roughness on the scattering properties of hexagonal columns with sizes from the Rayleigh to the geometric optics regimes, Journal of Quantitative Spectroscopy and Radiative Transfer, 129, 169–185, https://doi.org/10.1016/j.jqsrt.2013.06.011, 2013.

Lynch, D. K.: Cirrus clouds: Their role in climate and global change, Acta Astronautica, 38, 859–863, https://doi.org/10.1016/S0094-5765(96)00098-7, 1996.

Macke, A., Mueller, J., and Raschke, E.: Single Scattering Properties of Atmospheric Ice Crystals, Journal of the Atmospheric Sciences, 53, 2813–2825, https://doi.org/10.1175/1520-0469(1996)053<2813:SSPOAI>2.0.CO;2, 1996.

Mie, G.: Beiträge zur Optik trüber Medien, speziell kolloidaler Metallösungen, Annalen der Physik, 330, 377–445, https://doi.org/10.1002/andp.19083300302, 1908.

Mitchell, D. L.: Use of Mass- and Area-Dimensional Power Laws for Determining Precipitation Particle Terminal Velocities, Journal of the Atmospheric Sciences, 53, 1710–1723, https://doi.org/10.1175/1520-0469(1996)053<1710:UOMAAD>2.0.CO;2, 1996.

Microspheres | Thermo Fisher Scientific: https://www.thermofisher.com/search/browse/category/us/en/90220126, last access: 1 June 2024.

Paltridge, G. W.: Cloud-radiation feedback to climate, Quarterly Journal of the Royal Meteorological Society, 106, 895–899, https://doi.org/10.1002/qj.49710645018, 1980.

Sassen, K., Wang, Z., and Liu, D.: Global distribution of cirrus clouds from CloudSat/Cloud-Aerosol Lidar and Infrared Pathfinder Satellite Observations (CALIPSO) measurements, Journal of Geophysical Research: Atmospheres, 113, https://doi.org/10.1029/2008JD009972, 2008.

Schmitt, C. G. and Heymsfield, A. J.: On the Occurrence of Hollow Bullet Rosette– and Column-Shaped Ice Crystals in Midlatitude Cirrus, Journal of the Atmospheric Sciences, 64, 4514–4519, https://doi.org/10.1175/2007JAS2317.1, 2007.

Schmitt, C. G., Iaquinta, J., and Heymsfield, A. J.: The Asymmetry Parameter of Cirrus Clouds Composed of Hollow Bullet Rosette–Shaped Ice Crystals from Ray-Tracing Calculations, Journal of Applied Meteorology and Climatology, 45, 973–981, https://doi.org/10.1175/JAM2384.1, 2006.

Schnaiter, M., Järvinen, E., Abdelmonem, A., and Leisner, T.: PHIPS-HALO: the airborne particle habit imaging and polar scattering probe – Part 2: Characterization and first results, Atmospheric Measurement Techniques, 11, 341–357, https://doi.org/10.5194/amt-11-341-2018, 2018.

https://doi.org/10.5194/egusphere-2024-3316
Preprint. Discussion started: 4 November 2024

Schön, R., Schnaiter, M., Ulanowski, Z., Schmitt, C., Benz, S., Möhler, O., Vogt, S., Wagner, R., and Schurath, U.: Particle Habit Imaging Using Incoherent Light: A First Step toward a Novel Instrument for Cloud Microphysics, J. Atmos. Oceanic Technol., 28, 493–512, https://doi.org/10.1175/2011JTECHA1445.1, 2011.

Tang, G., Panetta, R. L., Yang, P., Kattawar, G. W., and Zhai, P.-W.: Effects of ice crystal surface roughness and air bubble inclusions on cirrus cloud radiative properties from remote sensing perspective, Journal of Quantitative Spectroscopy and Radiative Transfer, 195, 119–131, https://doi.org/10.1016/j.jqsrt.2017.01.016, 2017.

Um, J. and McFarquhar, G. M.: Single-Scattering Properties of Aggregates of Bullet Rosettes in Cirrus, Journal of Applied Meteorology and Climatology, 46, 757–775, https://doi.org/10.1175/JAM2501.1, 2007.

Um, J. and McFarquhar, G. M.: Dependence of the single-scattering properties of small ice crystals on idealized shape models, Atmospheric Chemistry and Physics, 11, 3159–3171, https://doi.org/10.5194/acp-11-3159-2011, 2011.

Um, J., McFarquhar, G. M., Hong, Y. P., Lee, S.-S., Jung, C. H., Lawson, R. P., and Mo, Q.: Dimensions and aspect ratios of natural ice crystals, Atmospheric Chemistry and Physics, 15, 3933–3956, https://doi.org/10.5194/acp-15-3933-2015, 2015.

Warren, S. G.: Optical constants of ice from the ultraviolet to the microwave, Appl. Opt., AO, 23, 1206–1225, https://doi.org/10.1364/AO.23.001206, 1984.

Weickmann, H. K.: Die Eisphase in der Atmosphäre, Royal Aircraft Establishment, 96, 1947.

White, F. M.: Viscous Fluid Flow, 3rd edition., McGraw Hill, New York, NY, 656 pp., 2005.

Wylie, D. P., Menzel, W. P., Woolf, H. M., and Strabala, K. I.: Four Years of Global Cirrus Cloud Statistics Using HIRS, Journal of Climate, 7, 1972–1986, https://doi.org/10.1175/1520-0442(1994)007<1972:FYOGCC>2.0.CO;2, 1994.

Xu, G., Schnaiter, M., and Järvinen, E.: Accurate Retrieval of Asymmetry Parameter for Large and Complex Ice Crystals From In-Situ Polar Nephelometer Measurements, Journal of Geophysical Research: Atmospheres, 127, e2021JD036071, https://doi.org/10.1029/2021JD036071, 2022.

Xu, G., Waitz, F., Wagner, S., Nehlert, F., Schnaiter, M., and Järvinen, E.: Ice Crystal Morphological Complexity and Asymmetry Parameter: Implications for Light Scattering Measurement, 2022.

Xu, G., Waitz, F., Wagner, S., Nehlert, F., Schnaiter, M., and Järvinen, E.: Toward Better Constrained Scattering Models for Natural Ice Crystals in the Visible Region, Journal of Geophysical Research: Atmospheres, 128, e2022JD037604, https://doi.org/10.1029/2022JD037604, 2023.

Yang, P. and Liou, K. N.: Single-scattering properties of complex ice crystals in terrestrial atmosphere, Contributions to Atmospheric Physics, 71, 1998.

Yang, P., Bi, L., Baum, B. A., Liou, K.-N., Kattawar, G. W., Mishchenko, M. I., and Cole, B.: Spectrally Consistent Scattering, Absorption, and Polarization Properties of Atmospheric Ice Crystals at Wavelengths from 0.2 to 100 μm, Journal of the Atmospheric Sciences, 70, 330–347, https://doi.org/10.1175/JAS-D-12-039.1, 2013.

Yang, P., Zhang, Z., Kattawar, G. W., Warren, S. G., Baum, B. A., Huang, H.-L., Hu, Y. X., Winker, D., and Iaquinta, J.: Effect of Cavities on the Optical Properties of Bullet Rosettes: Implications for Active and Passive Remote Sensing of Ice Cloud Properties, Journal of Applied Meteorology and Climatology, 47, 2311–2330, https://doi.org/10.1175/2008JAMC1905.1, 2008.